Liu, Junting ; Khayrudinov, Vladislav; Yang, He; Sun, Yue; Matveev, Boris ; Remennyi, Maxim; Yang, Kejian ; Haggren, Tuomas; Lipsanen, Harri; Wang, Fengqiu; Zhang, Baitao; He, Jingliang

InAs-Nanowire-based Broadband Ultrafast Optical Switch

Published in:
Journal of Physical Chemistry Letters

DOI:
10.1021/acs.jpclett.9b01626

Published: 18/07/2019

Document Version
Peer-reviewed accepted author manuscript, also known as Final accepted manuscript or Post-print

Please cite the original version:
Liu, J., Khayrudinov, V., Yang, H., Sun, Y., Matveev, B., Remennyi, M., Yang, K., Haggren, T., Lipsanen, H., Wang, F., Zhang, B., & He, J. (2019). InAs-Nanowire-based Broadband Ultrafast Optical Switch. *Journal of Physical Chemistry Letters*, *10*(15), 4429-4436. https://doi.org/10.1021/acs.jpclett.9b01626

InAs-Nanowire-based Broadband Ultrafast Optical Switch

Junting Liu[†], Vladislav Khayrudinov[‡], He Yang[, ‡], Yue Sun [§], Boris Matveev [∥], Maxim Remennyi [∥], Kejian Yang[†], Tuomas Haggren[‡], Harri Lipsanen[‡], Fengqiu Wang [§], Baitao Zhang[*, †] and Jingliang He[†]*

[†] State Key Laboratory of Crystal Materials, Institute of Crystal Materials, Shandong University, Shandong Jinan, 250100, China
[‡] Department of Electronics and Nanoengineering, Aalto University, Espoo, FI-00076, Finland
[§] School of Electronic Science and Engineering, Nanjing University, 210023, China
[∥] Loffe Institute, St. Petersburg, 194021, Russia

AUTHOR INFORMATION

Corresponding Author

[*]yhyanghe@gmail.com.[*]btzhang@sdu.edu.cn.

ABSTRACT. Due to their tunable optical properties with various shapes, sizes and compositions, nanowires (NWs) have been regarded as a class of semiconductor nanostructures with great potential for photodetectors, light-emitting diodes, gas sensors, microcavity lasers, optical modulators and converters. Indium arsenide (InAs), an attractive III-V semiconductor NW with the advantages of narrow bandgap and large electron mobility, has attracted considerable interest in infrared optoelectronic and photonic devices. Here, we studied the ultrafast carrier dynamics and nonlinear optical responses of InAs NWs ranging from 1.0 to 2.8 μm, and demonstrated the InAs-NW-based ultrafast broadband optical switch for passively Q-switching in all-solid-state laser systems. Furthermore, we achieved ultrafast optical modulation for laser mode-locking at 1.0 μm, paving the way for their applications in the field of ultrafast optics. These exotic optical

properties indicate that InAs NWs have significant potential for various optoelectronic and photonic devices, especially in the mid-infrared wavelength range.

TOC GRAPHICS

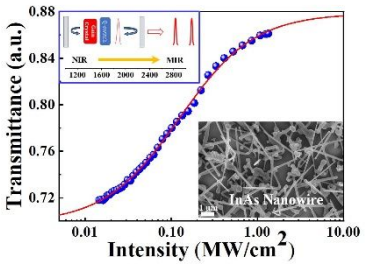

KEYWORDS: semiconductor nanowires, nonlinear absorption, ultrafast optical switch

In the past two decades, nanomaterials have attracted enormous research interest due to their fascinating structure-dependent optical and electrical properties [1-5], which have a significant impact on the realization of various photonic devices [6-8]. Due to their intrinsic quantum-confined one-dimensional (1D) structure, semiconductor nanowires (NWs) have been intensively studied as building blocks for the fabrication of nanoelectronic [9-11] and photonic [5, 12, 13] devices. Interestingly, the electrical and optical properties of semiconductor NWs can be tuned by controlling their sizes, shapes, and compositions. Therefore, semiconductor NWs provide a unique platform for tailoring light-matter interactions at the nanoscale and investigating the generation, amplification, propagation, detection, and modulation of light. Because of Lorentz local field effect, semiconductor NWs have

a larger nonlinear susceptibility compared to their bulk form [14, 15]. In addition, NW growth has a larger tolerance for lattice mismatch than thin-film epitaxial growth, resulting in more flexibility in the substrate selection and mechanical properties, which benefits to the effective modulation of the optical nonlinear susceptibility by external bending or twisting strains [16, 17].

III-V semiconductor NWs have been applied for various optoelectronic devices owing to large electron g-factors and small electron effective mass [18-20]. As the representative III-V semiconductor, indium arsenide (InAs) has a number of advantages, including high room-temperature electron mobility, low electronic effective loss and strong spin-orbit interaction [21, 22], which make it an attractive candidate for NW-based electronic and photonic devices. Indeed, high-performance single-electron transistors, resonant tunneling diodes, Josephson junctions and all-optical logic gates have been realized using InAs NWs [23-26]. Moreover, with the increase of the diameter, the bandgap of the InAs NW decreases and shifts from an indirect to a direct one [27]. The intrinsic unique band structure results in broadband optical conductivity and is useful for a tunable light-matter interaction over a broad wavelength range [22]. However, the investigation of their ultrafast dynamics, third-order nonlinear optical response, and ultrafast optic modulation properties have been rarely studied.

Here, we studied the ultrafast carrier dynamics and nonlinear optical response

of InAs NWs using pump-probe and open-aperture Z-scan techniques, and demonstrated the InAs-NW-based all-solid-state passively Q-switched and mode-locked lasers. The broadband optical properties in terms of ultrafast carrier relaxation dynamics and nonlinear optical absorption (saturable intensity and modulation depth) show the potential of InAs NWs for an application in optical switching with the operational wavelength up to 2.8 μm. Based on an InAs NW saturable absorber (SA), the shortest pulse widths of 411, 452 and 347 ns are obtained for passively Q-switched lasers operating at 1.06 μm, 1.94 μm, and 2.79 μm, respectively. Moreover, a passive mode-locking laser at 1.04 μm is demonstrated with the shorted pulse width of 349 fs. This is the best mode-locking performance based on NW SA reported so far. In addition, the fabrication of 1D NWs with different sizes, shapes and compositions by our growth method will provide more alternatives for the applications in various optoelectronic devices.

The InAs NW samples used in this study were grown on quartz substrates by a self-catalyzed growth method inside a horizontal flow atmospheric pressure metal organic vapour phase epitaxy (MOVPE) system (see the details in the Methods section [28]). The high-resolution scanning electron microscopy (SEM) image in Figure 1 (a) shows that the lengths of NWs uniformly deposited on the quartz substrate reach ~7-9 μm with the density of ~5 NWs in 1μm^2, which is beneficial for their optical applications. The Figure 1 (b) shows that the as-grown NWs have

an average diameter of approximately 100 nm with smooth surfaces (see also Figure S1 (a) in the Supporting Information). A Raman spectrum of the NWs excited by a laser source operating at 473 nm is shown in Figure S1 (b). The two typical Raman peaks are identified as a transverse optical (TO) phonon mode and a longitudinal optical (LO) phonon mode located at 218.6 and 239.5 cm^{-1}, respectively, which are consistent with previous research [29]. To study the crystal structure of our InAs NWs, we did the analysis by high-resolution scanning transmission electron microscopy (HRSTEM) and energy-dispersive X-ray spectroscopy (EDX) measurements. As shown in Figure 1 (c), the structure of the InAs NWs is predominantly zinc-blend (ZB), which matches well with the results of Refs.[22, 30]. The EDX spectra in Figure S1 (c) shows that the NW body consists solely of In and As with no additional elements, which illustrates the high quality of our NW sample. To verify the bandgap of our InAs NWs, photoluminescence (PL) measurement was performed at room temperature (300 K) and low temperature (77 K). As shown in Figure 1 (d), only one PL peak appeared centering at 0.41 eV at low temperature (0.37 eV at room temperature), which corresponds to the band-to-band transition in bulk, that is ZB structure. The PL spectra of more NWs grown with different temperature on different substrates are presented Figure S2. In addition, the transmittance of the InAs NW sample was measured over the range of 900 to 3000 nm, as illustrated in Figure S3. The absorption is almost constant

from the near-infrared (NIR) to mid-infrared (MIR) regions, with a high absorptivity of 16.4% (subtracting the loss of the quartz substrate), indicating the excellent broadband optical absorption properties. The fluctuating absorbance peaks at approximately 2.7 μm might be caused by water vapor and atmospheric CO_2 absorption [31].

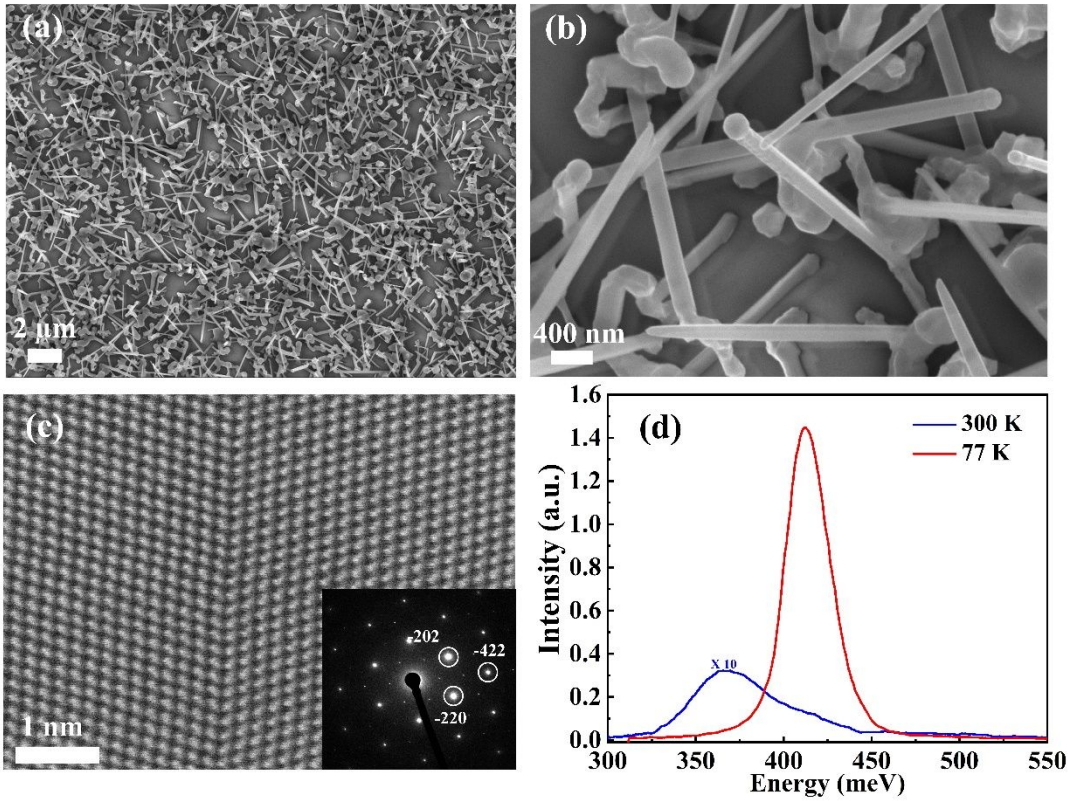

Figure 1. Optical and electron microscopy characterization of InAs NWs sample. (a) SEM image of as-prepared InAs sample with high density grown on a piece of quartz substrate. (b) A higher-resolution SEM image, which shows the diameter of our NWs at ~100 nm. (c) HRSTEM image of InAs NWs towards [110] zone axis. The inset diffraction pattern (towards [111] zone axis) clearly shows the ZB crystal

structure. (d) PL emission from InAs NW samples on a quartz substrate at room temperature (300 K) and low temperature (77 K).

Ultrafast carrier dynamics in various semiconductors play a significant role in their optoelectronic applications. In our work, a nondegenerate ultrafast pump-probe measurement was carried out to explore the ultrafast optical excited carrier dynamics of InAs NWs. The schematic experimental setup is shown in Figure S4 (details in the Methods section). As shown in Figure 2 (a)-(c), with the pump laser operating at 400 nm, the transient optical responses at three wavelengths centered at 1.0, 2.0 and 2.8 μm were detected by measuring the time-dependent normalized transmission ($^{\Delta T}/_{T_0}$) changes of the InAs NWs at room temperature. Here, T_0 is the transmittance of the probe laser beam before the pump laser excitation, and ΔT is the corresponding variation in the probe transmission after being excited by the pump laser. The positive $^{\Delta T}/_{T_0}$ signal reveals photobleaching signatures caused by Pauli blocking effects, which are induced by an excitation based on hot carrier dynamics. This indicates that InAs NWs exhibit a broadband saturable absorption effect in the wavelength band from 1.0 to 2.8 μm. As a reference, a piece of pure quartz substrate was subjected to the same measurement. No transient response was detected, indicating that the dynamical response was solely due to the InAs NWs.

For non-degenerate pump-probe measurements, the measured $\Delta T/T_0$ delay kinetics can be fitted to an exponential decay function [32]:

$$\frac{\Delta T}{T_0} = A_1 + A_2 \exp(-t/\tau) \qquad (1)$$

Here, A_1 and A_2 are the relative amplitudes of the double temporal components, and τ is attributed to inter-band carrier-photon coupling and electron-hole recombination. By using Eq. (1), τ was determined to be 2.07, 7.11 and 8.82 ps, respectively, for the probe wavelengths at 1.0, 2.0 and 2.8 μm. The picosecond decay time scale indicates that electron-phonon scattering dominates the decay processes, which is comparable to the slow decay time of graphene (1.5-5 ps) [33]. The ultrafast transient spectroscopy indicates that the InAs NWs exhibit ultrafast saturable absorption in the broadband range from 1.0 to 2.8 μm, while the corresponding ultrafast recovery time indicates it can be used for ultrafast optical signal processes, e.g., optical modulator, SA, and so on.

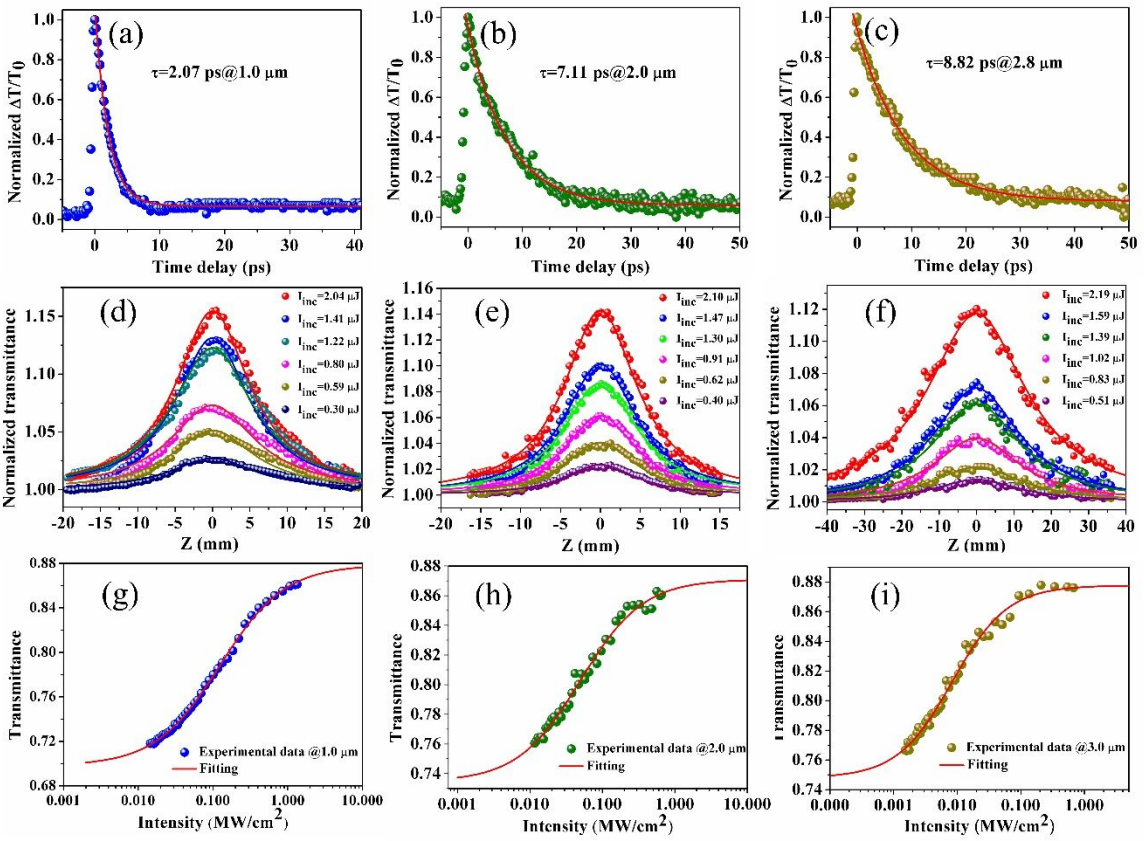

Figure 2. Characterization of the nonlinear optical absorption properties of InAs NWs. (a)-(c) show the ultrafast transient of InAs NWs with the probe wavelength at 1.0 μm, 2.0 μm and 2.8 μm by our home-made pump-probe setup. (d)-(f) show the saturation absorption properties at three wavelengths under different pump intensities. In these three figures, the dots are the collected experimental data, and the lines are the fittings. (g)-(i) illustrate the nonlinear transmittance at 1.0, 2.0 and 2.8 μm measured by our home-made open-aperture Z-scan setup.

To study the nonlinear optical absorption properties of InAs NWs, open-aperture Z-scan measurements were performed with excited lasers centered at

wavelengths of 1.0, 2.0 and 2.8 μm. Figure 2 (d)-(f) shows the intensity-dependent normalized transmittances as a function of the z position at the three wavelengths. The light transmittance increases with the increasing incident laser beam intensity. For a certain incident laser energy, the transmittance curve has a Gaussian-like shape that is symmetrical at the focus point (z =0), which clearly shows the saturable absorption property of the InAs NWs. According to nonlinear optical theory, light attenuation during propagation in a nonlinear optical medium can be described as [34]:

$$\frac{\mathrm{d}I}{\mathrm{d}z'} = -\alpha(I)I \qquad (2)$$

where I is the laser beam intensity, z' is the propagating distance in the material, and $\alpha(I)$ is the total absorption coefficient, which can be described in detail as [34, 35]

$$\alpha(I) = \alpha_0 + \beta_{eff} I \qquad (3)$$

where α_0 and β_{eff} are the linear and nonlinear absorption coefficients, respectively. By fitting the Z-scan measurement data in Figure 2 (d)-(f) using Eqs. (2) and (3), β_{eff} can be obtained as a function of the incident pulse energy, as shown in Figure 3 (a). The results show that β_{eff} is -0.10, -0.13 and -0.11 cm/W at 1.0, 2.0 and 2.8 μm, respectively. Note that β_{eff} remains constant for different incident energies at a given excitation wavelength, indicating that the single-photon saturable absorption process dominates the nonlinear absorption process in our measurements. The values of β_{eff} are comparable to those of an InAs nanocrystal

embedded in a SiO_2 thin film (-0.077 cm/W at 633 nm) [36] and much larger than those of most 2D materials, such as graphene [37], most transition metal dichalcogenides (TMDs, e.g., MoS_2 and WS_2) [38-41], and black phosphorus (BP) [42], indicating a strong saturable absorption capability. For further analysis, the imaginary part of the third-order nonlinear optical susceptibility $\chi^{(3)}$ can be obtained from the formula [34]:

$$\mathrm{Im}(\chi^{(3)}) = \frac{2n_0^2\varepsilon_0 c^2}{3\omega}\beta_{eff} \quad (4)$$

where n_o is the linear refractive index, ε_0 is the vacuum permittivity, c is the vacuum light speed, and ω is the angular frequency. The calculated $\mathrm{Im}(\chi^{(3)})$ is shown in Figure 3 (b), which shows a similar trend as β_{eff} with the values of -3×10^{-12}, -9×10^{-12} and -10.5×10^{-12} m^2/V^2 for the three above wavelengths, respectively. For comparison, we summarize β_{eff} and $\mathrm{Im}(\chi^{(3)})$ of several 2D materials and our InAs NWs in Table 1.

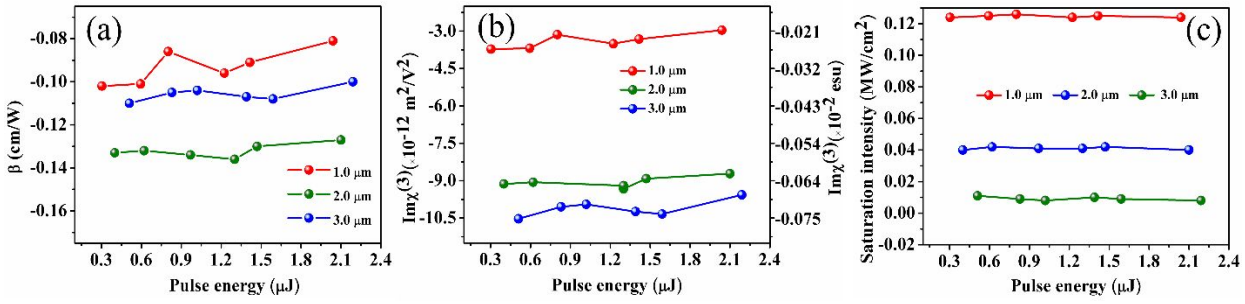

Figure 3. Analysis on the nonlinear optical parameters of InAs NWs. (a) concludes the nonlinear optical absorption coefficient of InAs NWs at three wavelengths, which is extracted from our Z-scan data. (b) shows the calculated imaginary part

of the third-order nonlinear optical susceptibility of InAs NWs, which provides useful information for the analysis of the intrinsic optical properties of InAs NWs. (c) shows the saturation intensity of InAs at three wavelengths under various pump energies.

Relatively larger β_{eff} in our measurements may be due to the pulse width of the excitation laser that is used (100 ns at 1.0, 2.0 and 2.8 μm). The saturable absorption principle of InAs NWs is based on the Pauli blocking effect, where the conduction band is fully occupied by accumulated excited carriers and cannot accept any more incoming carriers before relaxation. For the same InAs NW sample, the excited carrier density in the saturable state is always the same. Therefore, considering the ultrafast dynamics and relaxation time of the InAs NWs, the saturable intensity (I_s) for a ns excitation laser is much smaller than that of ps and fs excited lasers. Considering the saturable absorption, the total nonlinear absorption coefficient $\alpha(I)$ can be written as [43]

$$\alpha(\mathrm{I}) = \frac{\alpha_0}{1 + I/I_s} \qquad (5)$$

where I_s is the saturable intensity. Combining Eqs. (3) and (5), one can obtain

$$\alpha_0 + \beta_{eff} I = \frac{\alpha_0}{1 + I/I_s} \qquad (6)$$

For saturable absorption, the sign of β_{eff} is negative. Therefore, the absolute value of β_{eff} is larger for a lower saturable intensity.

To obtain the SA parameters, we fitted the Z-scan data by the following equation [30]:

$$T = \left(1 - \frac{\Delta R \times I_s}{I_0 \Big/ \left(I_s + \left(1 + \frac{z^2}{z_0^2}\right)\right)}\right) / (1 - \Delta R) \qquad (7)$$

where T is the transmittance, ΔR is the modulation depth, I_0 is the incident pulse intensity, and Z_0 is the diffraction length of the beam. From Figure 2 (d-f), we can see that the fitted lines match well with the experimental data. The corresponding nonlinear transmission curves versus the incident laser intensity at the three wavelengths are shown in Figure 2 (g-i). The resulting modulation depths were determined to be 16.7%, 14%, and 12.7%, while the averaged saturation intensities I_s were 0.13, 0.03 and 0.01 MW/cm^2 at 1.0, 2.0 and 2.8 μm, respectively. The saturable intensity as a function of the incident laser intensity is shown in Figure 3 (c). For a two-level system, the saturation intensity is proportional to the photon energy $h\nu$ ($I_S = h\nu/\sigma_A\tau$) and can be regarded as the upper limit of the SA. Here, σ_A is the absorption cross-section, and τ is the relaxation time. InAs NWs feature the highest saturation intensity and modulation depth at 1.0 μm, which is smaller or comparable to those of graphene [44], carbon nanotubes [45], TMDs [46], and BP [42].

After studying the saturable absorption properties of the InAs NWs, the related physical parameters of the ground-state (σ_{gs}) and excited-state (σ_{es}) cross-

sections are analysed based on the two-level energy band structure, which is vital for the realization of Q-switched and mode-locked lasers. A smaller σ_{gs}/σ_{es} ratio in nonlinear nanomaterials is helpful for the realization of saturable absorption, as it is easier for the excited state to be fully occupied. In this work, we calculated the ratio between σ_{gs} and σ_{es} by combining the following two equations [47, 48]:

$$\sigma_{gs} = \frac{-\ln T_0}{NL} \qquad (8)$$

$$\sigma_{es} = \frac{-\ln T_{max}}{NL} \qquad (9)$$

where N, T_0 and T_{max} are the ground-state carrier density, transmission in the linear regime and high-intensity saturated transmission, respectively. Based on the equations, the ratio of σ_{gs}/σ_{es} is determined to be 0.44, 0.47 and 0.57 at 1.0, 2.0 and 2.8 μm, respectively, indicating that InAs NWs are promising to work as SAs for the realization of pulsed lasers (e.g., mode-locked lasers).

To experimentally demonstrate the broadband saturable absorption properties of the InAs NWs, we designed passively Q-switched lasers with three different gain crystals with emission at 1.06, 1.94 and 2.79 μm. The passively Q-switched experimental setup is shown in Figure S5, and detailed information is given in the Methods section. After inserting the InAs NWs SA into the cavity, by adjusting the cavity mirror and the incident pump power, passive Q-switching was achieved at the three abovementioned. The relationship between the continuous-wave (CW) and passive Q-switched (PQS) average output power and the absorbed pump

power is illustrated in Figure S6 (b), S7 (b) and S8 (b). The highest average PQS output powers at 1.0, 2.0 and 2.8 μm were determined to be 343, 267 and 101 mW with slope efficiencies of 12%, 10.7% and 3.6%, respectively. The corresponding output power instabilities (RMS) were measured to be 1.75%, 2.02%, and 2.10% in 1 h at the maximum output power, and the corresponding beam quality factors M^2 were 1.16, 1.31 and 1.24, respectively.

The single pulse energy, peak power, pulse width and pulse repetition rate versus pump power at the three wavelengths are shown in Figure S6-S8. The single pulse energy, peak power and repetition rate of all the lasers increase with the increase of the absorbed pump power, while the pulse width decreases, which is typical for passively Q-switched lasers. The detailed output parameters for the maximum absorbed pump power are summarized in Table S1 in the Supporting Information. Figures 4 shows a typical pulse profile and the pulse train of the passively Q-switched lasers for the maximum incident pump power. The shortest pulse widths are 411, 452 and 347 ns with the highest repetition rates of 63, 63 and 55 kHz at 1.0, 2.0, and 2.8 μm, corresponding to the largest peak power of 13.28, 9.38 and 5.29 W and single pulse energy of 5.24, 4.44 and 1.84 μJ, respectively. The pulse-to-pulse instabilities were recorded and calculated to be 1.68%, 1.98% and 2.06% for the 1.0, 2.0, and 2.8 μm passive Q-switching lasers, respectively, which were consistent with the power instability.

According to the relationship between the output and intracavity power, the intracavity energy intensity I with the SA can be calculated by the following formula:

$$I = \frac{P_{out}(1 + R_{oc})}{f(1 - R_{oc})\pi r^2} \quad (10)$$

where P_{out} is the average output power, f is the repetition rate, R_{oc} is the reflection of the output mirror, and r is the radius of the oscillating laser mode with the SA. Based on the ABCD matrix, r was calculated to be 114, 156, and 240 μm at 1.0, 2.0, and 2.8 μm, respectively. Therefore, the corresponding maximum intracavity energy intensities for the InAs NWs were 520, 310 and 66.6 mJ/cm^2, respectively. This indicated that our InAs SA withstands a high damage threshold.

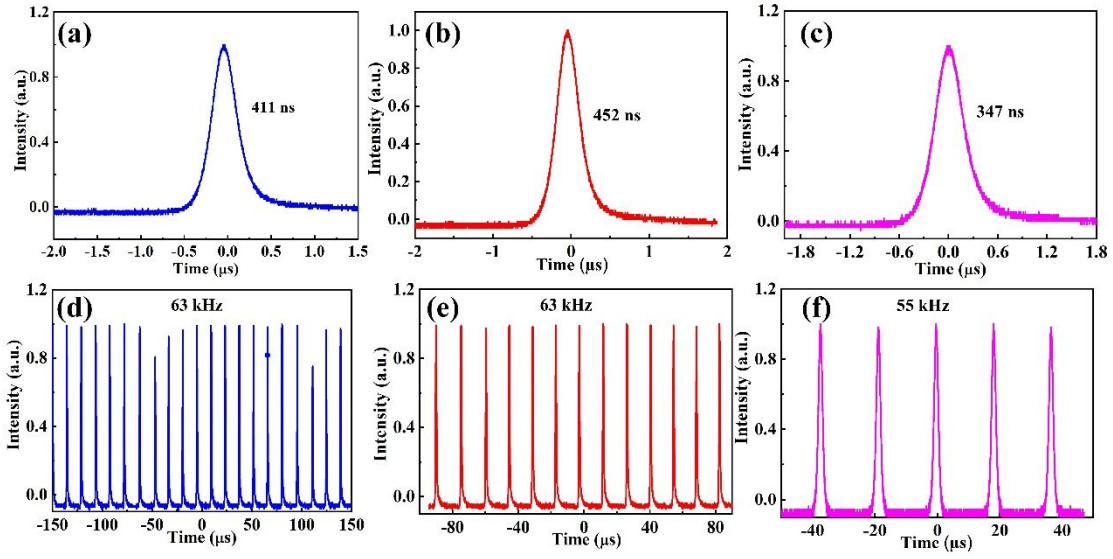

Figure 4. Laser diagnostics under the three wavelengths. (a)-(c) show the typical pulse profile of the passive Q-switched laser at the wavelength of 1.0, 2.0 and 2.8 μm, separately. (d)-(f) illustrate the corresponding passive Q-switched pulse trains.

To further study the saturable absorption of the InAs NWs and investigate their

ability to generate ultrashort pulses, a mode-locked solid-state laser was assembled and studied. A schematic of the mode-locked laser is shown in Figure S9, and the details are described in the Methods section. In ultrafast photonics applications of solid-state bulk lasers, the nonlinear saturable absorption of the SA is related to the Q-switched mode-locking instability status and thus blocks stable CW mode-locking. Stable CW mode-locking can be obtained only when the mode-locking pulse energy E_p is larger than the minimum intracavity pulse energy $E_{p,c}$, which can be expressed as [49]:

$$E_p^2 > E_{p,c^2} = F_{sat,A}A_{eff,\ A}F_{sat,L}A_{eff,L}\Delta R \qquad (11)$$

where $F_{sat,A}$ and $F_{sat,L}$ are the saturation fluences of the SA and laser crystal, respectively, and $A_{eff,\ A}$ and $A_{eff,L}$ are the effective laser mode areas of the SA and laser crystal. Considering the SA parameters, the equation can be expressed as:

$$\mathrm{F}_{sat,A}\Delta R < \frac{(PT_R)^2}{F_{sat,L}A_{eff,L}A_{eff,A}} = \frac{(PT_R)^2 \times m\sigma_{em,L}\lambda}{hc \times \pi\omega_{eff,L}^2 \times \pi\omega_{eff,A}^2} \qquad (12)$$

where P_{out} is the mode-locked output power, T_R is the round trip time, $\sigma_{em,L}$ is the emission cross-section of the laser crystal, λ is the laser wavelength, h is Planck constant, c is the light velocity, $\omega_{eff,A}$and $\omega_{eff,L}$ are the effective laser radii at the positions of the SA and laser crystal, respectively, and m is a cavity constant: m=1 for a ring cavity, and m=2 for a linear cavity. In our experiment, the emission cross-section $\sigma_{em,L}$ of the laser crystal is 3.1×10^{-20} cm^2, and T_R, $\omega_{eff,A}$ and $\omega_{eff,L}$ are determined to be ~23.6 ns, 39 μm and 28 μm, respectively. The left-hand side of Eq. (10), $F_{sat,A}\Delta R$ is calculated to be 0.162 mJ/cm^2, while the right-hand side is 0.199 mJ/cm^2 (at the threshold of the CW mode-locking operation P_{out}=244 mW). Therefore, stable CW mode-locked lasers can be obtained with the as-prepared InAs NWs SA and the as-designed laser cavity.

By inserting InAs NW device into the resonator, stable CW mode-locked

(CWML) operation was achieved when the absorbed pump power exceeded 6.15 W. The relationship between the absorbed pump power and the average output power is shown in Figure 5 (a). The CWML regime can be sustained until the absorbed pump power increased up to 7.20 W, corresponding to a maximum average output power of 504 mW. The output power instabilities (RMS) were measured to be less than 3% over 2 h.

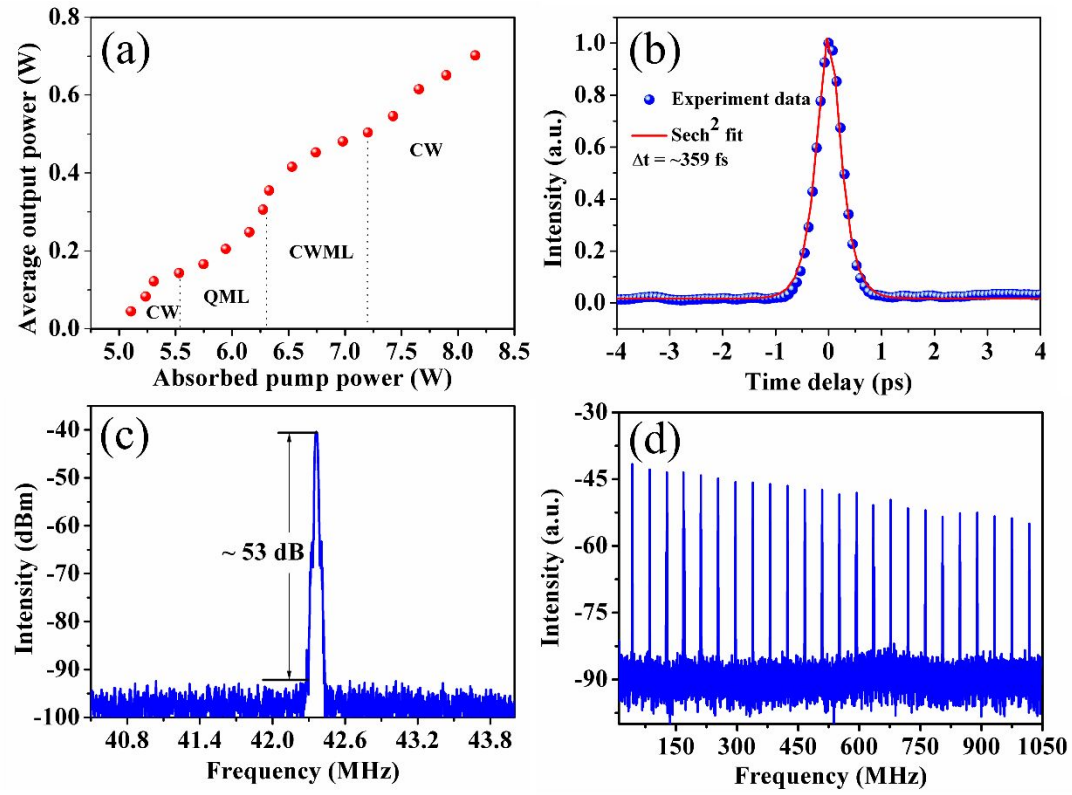

Figure 5. The mode-locked laser performance at 1.0 μm based on InAs SA. (a) The average output power under different pumped power. The running state of the output laser tuned under different pump intensities, which is clearly demonstrated inside. (b) The measured pulse width by autocorrelation spectroscopy is 349 fs. (c)

The recorded frequency spectrum of the mode-locked laser with a resolution bandwidth of 18 kHz. (d) The frequency spectrum over the 1.0 GHz wide-span.

As shown in Figure 5 (b), the pulse duration was measured to be 349 fs by $sech^2$

pulse shape fitting. The laser mode-locked at 1037.2 nm with a full width at half

maximum (FWHM) of 4.0 nm, corresponding to the time-bandwidth product of

0.398, as illustrated in Figure S10 (a). This value is larger than the Fourier-

transform-limited value (0.315), indicating that the output pulse is slightly chirped.

We recorded the CWML pulse trains at the maximum average output power with

time spans of 50 ns and 1 ms, as plotted in Figure S10 (b) and (c). The pulse trains

showed good amplitude stability with a pulse repetition rate of 42.36 MHz, which matched well with the cavity round trip time. The recorded radio frequency spectrum is shown in Figure 5(c), with a fundamental beat note near 42.36 MHz and a corresponding signal-to-noise ratio of 51 dB. In addition, there were no spurious frequency components or modulations over the entire 1.0 GHz span, as illustrated in Figure 5 (d). The absence of any spurious modulations proves the

Table 1. β_{eff} and the $Im\chi^{(3)}$ comparison between InAs NWs and 2D materials

Materials	Laser parameters	β_{eff} (cm*GW^{-1})	$Im\chi^{(3)}$ (esu)	Ref.
Graphene	800 nm, 1 kHz, 100 fs	-(1.52±0.4) ×10^{-2}	-(8.7±2.4) ×10^{-15}	[37]
$MoSe_2$	1064 nm, 10 kHz, 100 ps	-(2.05±0.17) ×10^{-2}	-(1.05±0.13) ×10^{-12}	[38]
MoS_2	800 nm, 1 kHz, 100 fs	-(2.42±0.8) ×10^{-2}	-(1.38±0.45) ×10^{-14}	[39]
WS_2	800 nm, 1 kHz, 40 fs	0.65 (RSA)	3.66×10^{-13}	[40]
WSe_2	1040 nm, 100 Hz, 340 fs	-(5.29±0.15) ×10^{3}	-(2.59±0.06) ×10^{-8}	[41]
BP	800 nm, 10 kHz	-1.38×10^{-2}	-7.85×10^{-15}	[42]
InAs NW	1064 nm, 50 kHz, 100 ns	-1.0 ×10^{8}	-2.2 ×10^{-4}	**This work**
InAs NW	2000 nm, 50 kHz, 100 ns	-1.3 ×10^{8}	-6.5 ×10^{-4}	**This work**
InAs NW	2800 nm, 50 kHz, 100 ns	-1.1×10^{8}	-7.4 ×10^{-4}	**This work**

clean CWML operation of the InAs NW fs pulsed laser. The fs pulsed laser parameters with different nanomaterials based on the SA at 1.0 μm are listed in Table S2, which indicate that InAs NW is a good SA candidate for ultrafast laser

generation.

In conclusion, here we prepared high-quality InAs NWs using self-catalyzed vapor-liquid-solid (VLS) method, which have distinctively broadband optical absorption properties. Using open-aperture Z-scan and non-degenerate pump-probe methods, we systematically studied their broadband (ranging from 1.0 to 2.8 μm) nonlinear optical absorption properties and carrier ultrafast dynamics, which provide a solid background for their application as optical switches and modulators. Furthermore, in the experiment, we demonstrated passively Q-switched all-solid-state lasers based on InAs NWs with the minimum pulse width of 347 ns at 2.8 μm. In addition, a femtosecond mode-locked solid-state laser based on InAs NWs was successfully achieved for the first time. Our studies pave the way for various high-quality NWs to be used in the future integrated photonic devices, which is useful for the realization of all-optical operation as a kind of nanoscale optical switches/modulators. In addition, we can easily tailor their optical properties by adjusting their growth conditions (e.g., temperature, growth time), which will broaden their applications in more various photonics devices.

ASSOCIATED CONTENT

Support Information

The Supporting Information is available free of charge on the ACS Publications website at DOI:*******. The supporting information is in pdf type and includes the

following contents.

AUTHOR INFORMATION

ORCID

He Yang: 0000-0003-3189-7298

Notes

The authors declare no competing financial interests.

ACKNOWLEDGMENTS

The authors acknowledge the funding from the National Research Foundation of China (61675116, 61575110), the Young Scholars Program of Shandong University (2017WLJH48), Academy of Finland Flagship Programme (320167, PREIN), Aalto University Doctoral School, Walter Ahlström Foundation, Nokia Foundation, and the Micronova Nanofabrication Centre of Aalto University.

REFERENCES

(1) Tans, S. J.; Verschueren, A. R.; Dekker, C. Room-temperature transistor based on a single carbon nanotube. *Nature* 1998, *393,* 49-52.

(2) Sun, D. M.; Timmermans, M. Y.; Tian, Y.; Nasibulin, A. G.; Kauppinen, E. I.; Kishimoto, S.; Mizutani, T.; Ohno, Y. Flexible high-performance carbon nanotube integrated circuits. *Nat. Nanotech. Nat. Nanotech.* 2011, *6,* 156-161.

(3) Bonaccorso, F.; Sun, Z.; Hasan, T.; Ferrari, A. Graphene photonics and

optoelectronics. *Nat. Photon.* **2010,** *4,* 611-622.

(4) Mak, K. F.; Shan, J. Photonics and optoelectronics of 2D semiconductor transition metal dichalcogenides. *Nat. Photon.* **2016,** *10,* 216-226.

(5) Yan, R.; Gargas, D.; Yang, P. Nanowire photonics. *Nat. Photon.* **2009,** *3,* 569-576.

(6) Li, Y.; Qian, F.; Xiang, J.; Lieber, C. M. Nanowire electronic and optoelectronic devices. *Mater. Today* **2006,** *9,* 18-27.

(7) Bao, Q.; Loh, K. P. Graphene photonics, plasmonics, and broadband optoelectronic devices. *ACS Nano* **2012,** *6,* 3677-3694.

(8) Wang, Q. H.; Kalantar-Zadeh, K.; Kis, A.; Coleman, J. N.; Strano, M. S. Electronics and optoelectronics of two-dimensional transition metal dichalcogenides. *Nat. Nanotech.* **2012,** *7,* 699-712.

(9) Yan, H.; Choe, H. S.; Nam, S.; Hu, Y.; Das, S.; Klemic, J. F.; Ellenbogen, J. C.; Lieber, C. M. Programmable nanowire circuits for nanoprocessors. *Nature* **2011,** *470,* 240-244.

(10) Yang, H.; Khayrudinov, V.; Dhaka, V.; Jiang, H.; Autere, A.; Lipsanen, H.; Sun, Z.; Jussila, H. Nanowire network–based multifunctional all-optical logic gates. *Sci. Adv.* **2018,** *4,* eaar7954.

(11) Zhang, A.; Zheng, G.; Lieber, C. M. *Nanowires: Building blocks for nanoscience and nanotechnology;* Springer Nature Press: Switzerland, 2016.

(12) Barrelet, C. J.; Greytak, A. B.; Lieber, C. M. Nanowire photonic circuit elements. *Nano Lett.* **2004,** *4,* 1981-1985.

(13) Cui, Y.; Wei, Q.; Park, H.; Lieber, C. M. Nanowire nanosensors for highly sensitive and selective detection of biological and chemical species. *Science* **2001,** *293,* 1289-1292.

(14) Zhuo, G. Y.; Hsu, K. J.; Su, T.-Y.; Huang, N. H.; Chen, Y. F.; Chu, S. W. Effect of Lorentz local field for optical second order nonlinear susceptibility in ZnO nanorod. *J. Appl. Phys.* **2012,** *111,* 103-112.

(15) Sanatinia, R.; Swillo, M.; Anand, S. Surface second-harmonic generation from vertical GaP nanopillars. *Nano Lett.* **2012,** *12,* 820-826.

(16) Han, X.; Wang, K.; Long, H.; Hu, H.; Chen, J.; Wang, B.; Lu, P. Highly sensitive detection of the lattice distortion in single bent ZnO nanowires by second-harmonic generation microscopy. *ACS Photonics* **2016,** *3,* 1308-1314.

(17) Jassim, N. M.; Wang, K.; Han, X.; Long, H.; Wang, B.; Lu, P. Plasmon assisted enhanced second-harmonic generation in single hybrid Au/ZnS nanowires. *Opt. Mater.* **2017,** *64,* 257-261.

(18) Wang, Z. L. *Nanowires and nanobelts: materials, properties and devices. Volume 1: Metal and Semiconductor Nanowires;* Springer Science & Business Media: New York, 2003.

(19) Johansson, J.; Karlsson, L. S.; Svensson, C. P. T.; Mårtensson, T.; Wacaser, B. A.; Deppert, K.; Samuelson, L.; Seifert, W. Structural properties of〈111〉B-oriented III–V nanowires. *Nat. Mater.* **2006,** *5,* 574-580.

(20) Lim, S. K.; Brewster, M.; Qian, F.; Li, Y.; Lieber, C. M.; Gradecak, S. Direct correlation between structural and optical properties of III− V nitride nanowire heterostructures with nanoscale resolution. *Nano Lett.* **2009,** *9,* 3940-3944.

(21) Dayeh, S. A.; Aplin, D. P.; Zhou, X.; Yu, P. K.; Yu, E. T.; Wang, D. High electron mobility InAs nanowire field-effect transistors. *Small* **2007,** *3,* 326-332.

(22) Galicka, M.; Bukała, M.; Buczko, R.; Kacman, P. Modelling the structure of GaAs and InAs nanowires. *J. Phys.: Condens. Matter.* **2008,** *20,* 454226.

(23) Liu, Z.; Luo, T.; Liang, B.; Chen, G.; Yu, G.; Xie, X.; Chen, D.; Shen, G. High-detectivity InAs nanowire photodetectors with spectral response from ultraviolet to near-infrared. *Nano Res.* **2013,** *6,* 775-783.

(24) Du, J.; Liang, D.; Tang, H.; Gao, X. P. InAs nanowire transistors as gas sensor and the response mechanism. *Nano Lett.* **2009,** *9,* 4348-4351.

(25) Jiang, X.; Xiong, Q.; Nam, S.; Qian, F.; Li, Y.; Lieber, C. M. InAs/InP radial nanowire heterostructures as high electron mobility devices. *Nano Lett.* **2007,** *7,* 3214-3218.

(26) Wang, C.; Chien, J.C.; Fang, H.; Takei, K.; Nah, J.; Plis, E.; Krishna, S.; Niknejad, A. M.; Javey, A. Self-aligned, extremely high frequency III–V metal-oxide-semiconductor field-effect transistors on rigid and flexible substrates. *Nano Lett.* **2012,** *12,* 4140-4145.

(27) Gordanian, E.; Jalali-Asadabadi, S.; Ahmad, I.; Rahimi, S.; Yazdani-Kachoei, M. Effects of dangling bonds and diameter on the electronic and optical properties of InAs nanowires. *RSC Adv*. **2015,** *5,* 23320-23325.

(28) Haggren, T.; Khayrudinov, V.; Dhaka, V.; Jiang, H.; Shah, A.; Kim, M.; Lipsanen, H. III-V nanowires on black silicon and low-temperature growth of self-catalyzed rectangular InAs NWs. *Sci. Rep.* **2018,** *8,* 6410.

(29) Tanta, R.; Lindberg, C.; Lehmann, S.; Bolinsson, J.; Carro-Temboury, M. R.; Dick, K. A.; Vosch, T.; Jespersen, T. S.; Nygård, Micro-Raman spectroscopy for the detection of stacking fault density in InAs and GaAs nanowires. J. *Phys. Rev. B* **2017,** *96,* 165433.

(30) Lide, D. R. *CRC handbook of chemistry and physics;* CRC Press: Boca Raton, 2004.

(31) Jiang, X.; Liu, S.; Liang, W.; Luo, S.; He, Z.; Ge, Y.; Wang, H.; Cao, R.; Zhang, F.; Wen, Q. Broadband Nonlinear Photonics in Few-Layer MXene Ti_3C_2Tx (T= F, O, or OH). *Laser. Photonics. Rev.* **2018,** *12,* 1700229.

(32) Prasankumar, R. P.; Taylor, A. J. *Optical techniques for solid-state materials characterization;* CRC Press: Boca Raton, 2016.

(33) Winnerl, S.; Göttfert, F.; Mittendorff, M.; Schneider, H.; Helm, M.; Winzer, T.; Malic, E.; Knorr, A.; Orlita, M.; Potemski, M. ime-resolved spectroscopy on epitaxial graphene in the infrared spectral range: relaxation dynamics and saturation behavior. *J. Phys. Condens. Mat.* **2013,** *25,* 054202.

(34) Wang, K.; Szydłowska, B. M.; Wang, G.; Zhang, X.; Wang, J. J.; Magan, J. J.; Zhang, L.; Coleman, J. N.; Wang, J.; Blau, W. J. Ultrafast nonlinear excitation dynamics of black phosphorus nanosheets from visible to mid-infrared. *ACS Nano* **2016,** *10,* 6923-6932.

(35) Feng, Y.; Dong, N.; Wang, G.; Li, Y.; Zhang, S.; Wang, K.; Zhang, L.; Blau, W. J.; Wang, J. Saturable absorption behavior of free-standing graphene polymer composite films over broad wavelength and time ranges. *Opt. Express* **2015,** *23,* 559-569.

(36) Shi, J.; Zhu, K.; Zhang, L. Nonlinear optical absorption of InAs nanocrystals embedded in SiO_2 thin films. *Solid. State. Commun.* **1999,** *110,*

645-649.

(37) Liu, Z. B.;Wang, Y.; Zhang, X. L.; Xu, Y. F.; Chen, Y. S.; Tian, J. G. Nonlinear optical properties of graphene oxide in nanosecond and picosecond regimes. *Appl. Phys. Lett.* **2009,** *94,* 021902 .

(38) Wang, K.; Feng, Y.; Chang, C.; Zhan, J.; Wang, C.; Zhao, Q.; Coleman, J. N.; Zhang, L.; Blau, W. J.; Wang, J. Broadband ultrafast nonlinear absorption and nonlinear refraction of layered molybdenum dichalcogenide semiconductors. *Nanoscale* **2014,** *6,* 10530-10535.

(39) Wang, K. P.; Wang, J.; Fan, J. T; Lotya, M.; Feng, Y. Y.; Zhang, X. Y.; Blau, W. J. Ultrafast Saturable Absorption of Two-Dimensional MoS2 Nanosheets. *ACS Nano* **2013,** *7,* 9260-9267.

(40) Wei, R. F.; Tian, X. L.; Zhang, H.; Hu, Z. L.; He, X.; Chen, Z.; Chen, Q. Q.; Qiu, J. R. Facile synthesis of two-dimensional WS_2 with reverse saturable absorption and nonlinear refraction properties in the PMMA matrix. *J. Alloy. Compd.* **2016,** *5,* 224-229.

(41) Dong, N. N.; Li, Y. X.; Zhang, S. F.; Zhang, X. Y.; Cui, Y.; Zhang, L.; Duesberg, G.; Wang, J. Dispersion of nonlinear refractive index in layered WS_2 and WSe_2 semiconductor films induced by two-photon absorption. *Opt. Lett.* **2016,** *17,* 3936-3939.

(42) Lu, S.; Miao, L.; Guo, Z.; Qi, X.; Zhao, C.; Zhang, H.; Wen, S.; Tang, D.; Fan, D. Broadband nonlinear optical response in multi-layer black phosphorus: an emerging infrared and mid-infrared optical material. *Opt. Express* **2015,** *23,* 11183-11194.

(43) Xing, G.; Guo, H.; Zhang, X. T.; Sum, C.; Huan, C. H. A. The Physics of ultrafast saturable absorption in graphene. *Opt. Express* **2010,** *18,* 4564–4573.

(44) Sun, Z.; Hasan, T.; Torrisi, F.; Popa, D.; Privitera, G.; Wang, F.; Bonaccorso, F.; Basko, D. M.; Ferrari, A. C. Graphene mode-locked ultrafast laser. *ACS Nano* **2010,** *4,* 803-810.

(45) Martinez, A.; Sun, Z. Nanotube and graphene saturable absorbers for fibre lasers. *Nat. Photon.* **2013,** *7,* 842-845.

(46) Luo, Z.; Wu, D.; Xu, B.; Xu, H.; Cai, Z.; Peng, J.; Weng, J.; Xu, S.; Zhu, C.; Wang, F. Two-dimensional material-based saturable absorbers: towards compact visible-wavelength all-fiber pulsed lasers. *Nanoscale* **2016,** *8,* 1066-1072.

(47) Yadav, R. K.; Sharma, R.; Aneesh, J.; Abhiramnath, P.; Adarsh, K. Saturable absorption in one-dimensional Sb_2Se_3 nanowires in the visible to near-infrared region. *Opt. Lett.* **2016,** *41,* 2049-2052.

(48) Burshtein, Z.; Blau, P.; Kalisky, Y.; Shimony, Y.; Kikta, M. Excited-state absorption studies of Cr/sup 4+/ions in several garnet host crystals. *IEEE. J. Quantum. Elect.* **1998,** *34,* 292-299.

(49) Keller, U. Recent developments in compact ultrafast lasers. *Nature* **2003,** *424,* 831-838.